Engineering the mechanical properties of graphene nanotube hybrid structures through structural modulation

K. Xia[1], H.F. Zhan[1], Y. Wei[1, 2], S.B. Sang[2], and *Y.T. Gu[1]

[1]School of Chemistry, Physics and Mechanical Engineering, Queensland University of Technology, Brisbane, Australia
[2]MicroNano System Research Center, Key lab of advanced Transducers and Intelligent Control System of the Ministry of Education & College of information Engineering, Taiyuan University of Technology, Taiyuan, China

*Corresponding author: yuantong.gu@qut.edu.au

Abstract

The excellent multi-functional properties of carbon nanotube (CNT) and graphene have enabled them as appealing building blocks to construct 3D carbon-based nanomaterials or nanostructures. The recently reported graphene nanotube hybrid structure (GNHS) is one of the representatives of such nanostructures. This work investigated the relationships between the mechanical properties of the GNHS and its structure basing on large-scale molecular dynamics simulations. It is found that increasing the length of the constituent CNTs, the GNHS will have a higher Young's modulus and yield strength. Whereas, no strong correlation is found between the number of graphene layers and Young's modulus and yield strength, though more graphene layers intends to lead to a higher yield strain. In the meanwhile, the presences of multi-wall CNTs are found to greatly strengthen the hybrid structure. Generally, the hybrid structures exhibit a brittle behavior and the failure initiates from the connecting regions between CNT and graphene. More interestingly, affluent formations of monoatomic chains and rings are found at the fracture region. This study provides an in-depth understanding of the mechanical performance of the GNHSs while varying their structures, which will shed lights on the design and also the applications of the carbon-based nanostructures.

Keywords: Graphene, Carbon nanotube, Tension, Molecular dynamics simulations

Introduction

In the past decade, low dimensional carbon-based nanomaterials, carbon nanotube (CNT) and graphene, have fascinated the scientific community with their excellent mechanical, electrical and thermal properties [Wang (2005); Zhu et al. (2010)]. Their appealing properties, e.g., Young's modulus up to 1 TPa, high fracture strength and low mass density, have enabled them with a wide promising applications in electronics, photonics, composite materials, energy storage, sensors, and bio-applications [Novoselov et al. (2012); De Volder et al. (2013); Dellinger et al. (2013)]. For example, a CNT-based mechanical mass sensor has been reported with a resolution of 1.7 yg (1 yg=10^{-24} g, corresponds to the mass of one proton) [Chaste et al. (2012)]. The enticing properties of carbon materials have driven the exploration of three-dimensional nanomateirals or nanostructures, such as the so-called "super" nanotubes or graphene that are made from CNTs [Coluci et al. (2006)], CNT bundles [Kis et al. (2004)], graphene/nanowire sandwich structures [Liu and Kuo (2013)], and the graphene nanotube hybrid structure (GNHS) [Zhu et al. (2012)].

The GNHS, as one of the representatives of the three-dimensional nanomaterials, has been envisioned with various potential applications in adsorption, biosensors, batteries, nanocomposite, drug delivery, and so on [Zhao et al. (2012); Odedairo et al. (2014)]. For instance, it is found that the GNHS can store up to 41 g H_2/L under ambient conditions with lithium cations doping [Dimitrakakis et al. (2008)]. Experiments show that the GNHS has a high specific capacitance and remarkable rate capability, which significantly outperform many electrode materials currently used

in the state-of-the-art supercapacitors [Du et al. (2011)]. Hernandez-Ferrer *et al.* [Hernández-Ferrer et al. (2014)] shows that the multi-walled CNT/graphene hybrid materials possess higher heterogeneous charge transfer constant and sensitivity towards H_2O_2 reduction, which is promising for the applications in electrochemical sensing.

Series of studies have been carried out on GNHSs to facilitate their diverse applications. For example, using first principle calculations, the conductance of the GNHS is found to nearly independent of the CNT length, but changes strongly with the link structure [Novaes et al. (2010)]. Molecular dynamics simulations have shown that the thermal transport of the GNHS is governed by the minimum CNT's distance and length, due to the scattering of phonons occurred at the CNT-graphene junctions [Varshney et al. (2010)], and the long-wavelength out-of-plane modes contribute significantly to thermal conduction [Loh et al. (2011)]. Using the phonon wave packet method, Lee *et al.* [Lee et al. (2012)] found that the graphene interface distributes the incoming phonon energy to both sides of the interface almost equally, and provides a strong diffusive scattering site. It is noticed that majority of current studies have focused on the electrical and thermal properties of the GNHS, and their mechanical properties are still lacking of investigation. One recent work reported the mechanical properties of four different GNHS basing on the structural molecular mechanics approach [Sihn et al. (2012)]. Though our pervious works have probed the mechanical properties of GNHS with different CNT allocations [Zhan et al. (2013)] and dopants [Xia et al. (2014)], a more comprehensive understanding of the structural impacts on the associated mechanical properties are still required.

Therefore, in this work, we will investigate how the tensile properties of the GNHS can be tailored through the structure variation by the large-scale molecular dynamics (MD) simulations. Experiments have already reported the controllable fabrication of the graphene nanotube hybrid structures *via* one-step chemical vapor deposition process [Paul et al. (2010)]. Emphasis will be laid on the mechanical properties (Young's modulus, yield strength and yield strain) of the GNHS under tensile loading. Different hybrid structures will be constructed by either varying the length of the single-wall CNTs (SWNTs) or the number of graphene layers.

Computational details

A series of large-scale MD simulations were performed using the open-source LAMMPS code [Plimpton (1995)]. All tested hybrid structures have a similar width around 5.6 nm. The hybrid structures are constructed by connecting an armchair (4,4)-CNT with graphene through heptagons (see Figure 1) [Matsumoto and Saito (2002); Dimitrakakis, Tylianakis et al. (2008); Varshney, Patnaik et al. (2010)]. To acquire the tensile properties of different hybrid structures, two groups of models have been established, including the GNHSs either with different CNT lengths or with different number of graphene layers. For discussion convenience, the GNHSs with different CNT lengths are denoted as GNHS-L#, where # ranges from 1 to 6 representing the CNT length ranging from 24.9 Å to 51.9 Å (these models possess two graphene layers). The GNHSs with different number of graphene layers are denoted as GNHS-N#, where # runs from 1 to 3 representing three, four and five graphene layers (see Figure 1b). All models will be constructed by single-wall CNTs (SWNTs), as shown in Figure 1.

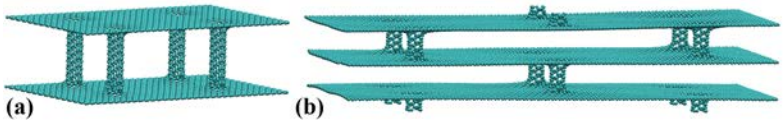

Figure 1. Simulation models of the graphene nanotube hybrid structures with: (a) two graphene layers; (b) three graphene layers.

To describe the interactions between carbon atoms, the popularly applied reactive empirical bond order (REBO) potential [Brenner et al. (2002)] was adopted, which has been shown to well represent the binding energy and elastic properties of graphene and CNT [Zhang et al. (2011)]. The whole simulation is carried out in three steps, including initial energy minimization using the conjugate gradient algorithm, relaxation under the NVT ensemble using Nose-Hoover thermostat [Nosé (1984); Hoover (1985)], and then tension of the sample. To minimize the thermal influence, a relatively low temperature, 1 K is used during the simulation. A time step of 1 fs is chosen, and the hybrid structure is relaxed for 500 ps. During the tensile deformation, one end of the GNHS was fixed, and a constant velocity of 0.001 Å/ps was applied to the other end along the length direction. The equations of motion are integrated with time using a Velocity Verlet algorithm [Verlet (1967)], with no periodic boundary conditions being applied.

During the simulation, the virial stress is applied to calculate the atomic stress $\Pi^{\alpha\beta}$ during tension, which is expressed as [Diao et al. (2004)]

$$\Pi^{\alpha\beta} = \frac{1}{\Omega}\sum_i \varpi_i \pi_i^{\alpha\beta}\ ,\ \pi_i^{\alpha\beta} = \frac{1}{\varpi_i}\left(-m_i v_i^{\alpha} v_i^{\beta} + \frac{1}{2}\sum_{j\neq i} F_{ij}^{\alpha} r_{ij}^{\beta}\right) \quad (1)$$

Here $\pi_i^{\alpha\beta}$ is the atomic stress associated with atom *i*. ϖ_i is the effective volume of the *i*th atom and Ω is the volume of the whole system. m_i and v_i are the mass and velocity of the *i*th atom, respectively. F_{ij} and r_{ij} are the force and distance between atoms *i* and *j*, respectively, and the indices α and β denote the Cartesian components. The engineering strain is used to estimate the strain as $\varepsilon = (l - l_0)/l_0$, where *l* and l_0 are the instantaneous and initial length of the sample.

Results and discussions

Impacts from the nanotube's length

In the beginning, we assess the tensile properties of GNHSs containing two layers that are pillared by SWNTs with different lengths. Six cases are considered, with the SWNT's length ranging from 24.9 to 58.2 Å (see Figure 1). Figure 2a shows the stress-strain curves obtained from MD simulations. Generally, all stress-strain curves share an identical changing trend, i.e., the stress increases linearly at the beginning, and decreases suddenly after passing a specific stress value. According to the continuum mechanics [Gere and Timoshenko (1999)], such stress-strain profile signifies that the GNHS exhibits a brittle behavior. Following previous researchers [Zhan and Gu (2011)], Young's modulus is derived directly from the stress-strain curve with the strain <3% using linear regression. The yield strength is referred to the peak stress after which the failure of the structure is observed. The corresponding strain is denoted as yield strain. For the GNHS with the CNT length of 24.9 Å, a Young's modulus of 187.9 GPa is estimated, with the yield strength and yield strain calculated as 19.2 GPa, and 10.7%, respectively.

It is observed from Figure 2a that the longer length of the SWNT, the lower Young's modulus and yield strength of the GNHS. For example, the GNHS constructed by the shortest SWNT (length of 24.9 Å) shows the highest Young's modulus which is almost two times of its counterpart with 51.9 Å SWNTs. According to Figure 2b, the effective Young's modulus of the GNHSs exhibits a linear relationship with the length of the SWNT. This phenomenon is understandable, as the effective atom volume is a linear function of the SWNT's length, which will thus lead to a linear reduction to the atomic stress, see Eq. (1). Therefore, it is reasonable to observe a linearly decreased Young's modulus and yield strength with the increasing SWNT's length. Additionally, we find that the yield strain for all considered samples appears almost the same (around 10.6%, consistent with the results

reported by other researchers [Xu et al. (2012)]), implying that the SWNT's length exerts ignorable influence on the yield strain. Such observations can be explained by considering that the elastic tensile deformation of different GNHS is dominated by the two (upper and lower, see Figure 1) graphene layers. In other words, regardless how the length of the SWNT changes, the graphene layers will absorb majority of the tensile strain energy while the GNHS is elongated along *the* length direction, and thus induce a similar yield strain.

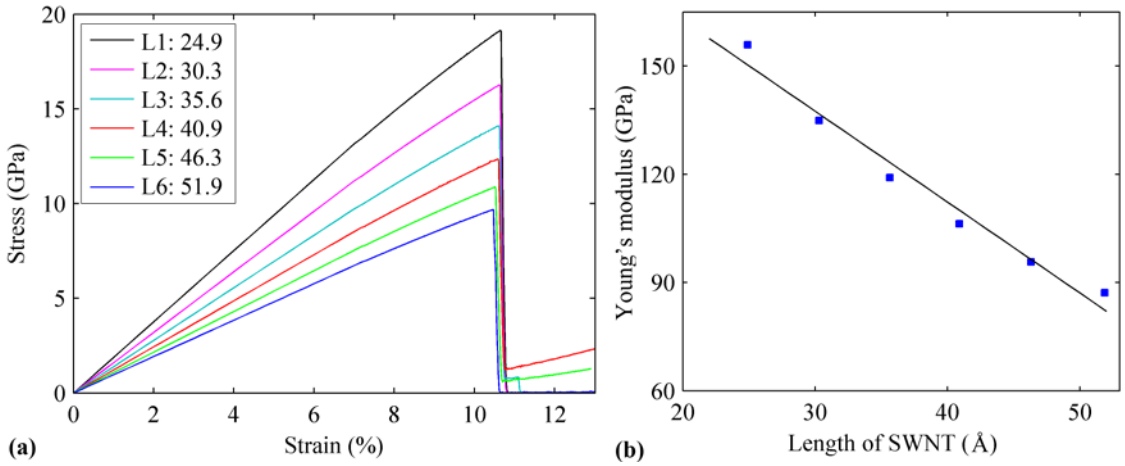

Figure 2. (a) Stress-strain curves of GNHS containing two graphene layers pillared by SWNT with different lengths; (b) The effective Young's modulus as a function of the SWNT's length.

To further investigate the impacts on the tensile properties of GNHS from the SWNT's length, we acquire the atomic configurations of the GNHS at different strains. In agreement with the stress-strain curves presented in Figure 2a, the atomic structure for all GNHSs show marginal changes during the elastic deformation period (before reaching the peak stress). After yielding, bond breakings are found. Generally, GNHS-L1, L2 and L3 share the same deformation behaviors. As illustrated in Figure 3a, during the elastic deformation period, the C-C bonds are stretched along the loading direction. With the increasing strain, fracture of the structure is observed, which is initiated from two CNT-graphene junctions (one on the top layer, the other on the bottom layer) between graphene layer and CNT near the two ends (Figure 3b). From Figure 3c, the structure is found to failure around two connecting regions with further extension. Particularly, after failure, local buckling of the graphene sheet due to the release of the strain as well as the inclined CNTs is observed. It is interesting to mention that at the front of the failure region, the formations of monoatomic chains (inset of Figure 3b) and monoatomic rings (inset of Figure 3c) are observed.

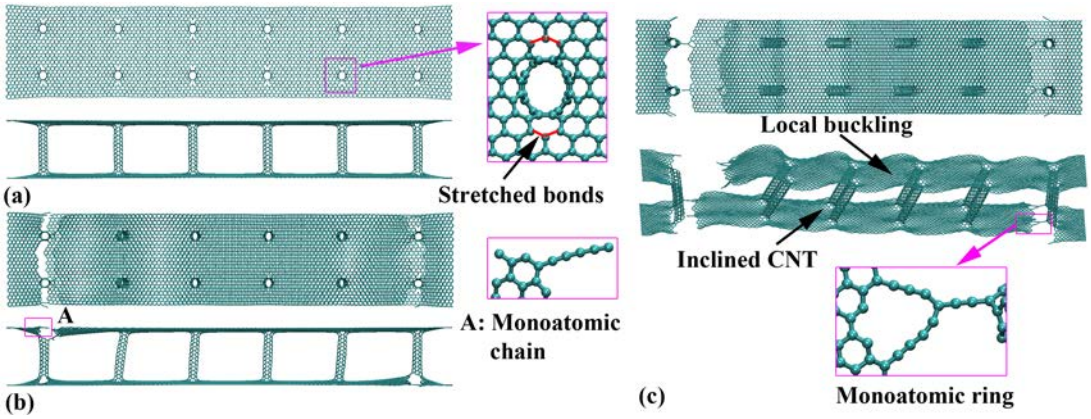

Figure 3. GNHS-L3 at the strain of: (a) 10.59%, inset shows the stretched C-C bonds around the CNT-graphene junction; (b) 10.65%, inset shows the formation of monoatomic chain; (c) 10.76%, inset shows the existence of monoatomic ring.

Similar deformation procure is also observed for the hybrid structure with longer CNTs (i.e., GNHS-L4 and GNHS-L5). As illustrated in Figure 4a, the CNT pillars appear a larger inclined angles due to the extension of the top and bottom graphene layers. The fracture is nucleated from the connecting regions and the graphene sheet is bulked after failure. The existence of monoatomic chains and rings are also observed (Figure 4b). Particularly, unlike the atomic configurations in Figure 3c, the top and bottom graphene layers are still connected by the inclined CNTs after failure for the GNHS-L4. Such phenomenon is consistent with the stress-strain curves in Figure 2a, from which the stress does not reduce directly to zero after failure. For the hybrid structure with the longest CNTs considered in this paper (GNHS-L6), a different deformation scheme is observed besides the monoatomic chains and rings emerged around the fracture region. As shown in Figure 4c, the fracture initiates from one end of the structure, which results in an early separation at the fracture region. In particular, the CNTs are still vertically aligned after yielding and a more evident local buckling of the graphene sheet is observed.

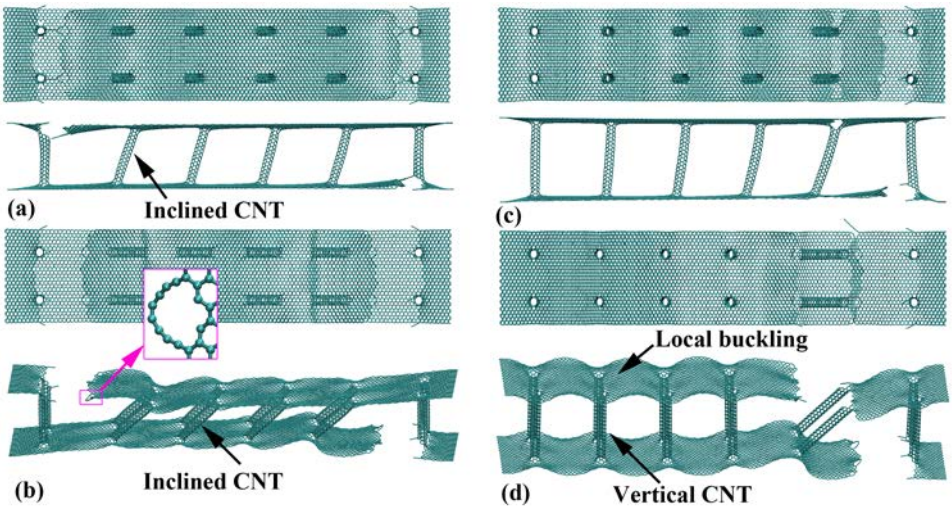

Figure 4. GNHS-L4 at the stain of: (a) 10.66%, (b) 10.74%, inset shows the formation of monoatomic chain; GNHS-L6 at the strain of: (a) 10.54%, (b) 10.64%.

Influence of the graphene layer number

Above discussions suggest that the increase of SWNT's length will result a direct reduction to the effective Young's modulus and yield strength of the hybrid structure. In this section, we investigate the influence on the tensile properties of GNHS from the number of graphene layers, i.e., the GNHS contains three, four and five graphene layers pillared by SWNTs (see Figure 1).

From Figure 5, the tensile properties of the GNHS vary with different number of graphene layers, and no explicit correlation is found between them. For example, comparing with the hybrid structure with two graphene layers, the GNHS-N1 (three-layers) shows a much smaller Young's modulus and yield strength, around 116.3 and 12.8 GPa, respectively. Whereas, increasing the number of graphene layers from three to four (GNHS-N2) yields a larger Young's modulus (139.6 GPa) and yield strength (16.2 GPa), and the hybrid structure with more graphene layers (GNHYS-N3) exhibit a similar tensile properties as estimated from GNHS-N2. In general, the yield strain is found to increase with the increasing number of graphene layers.

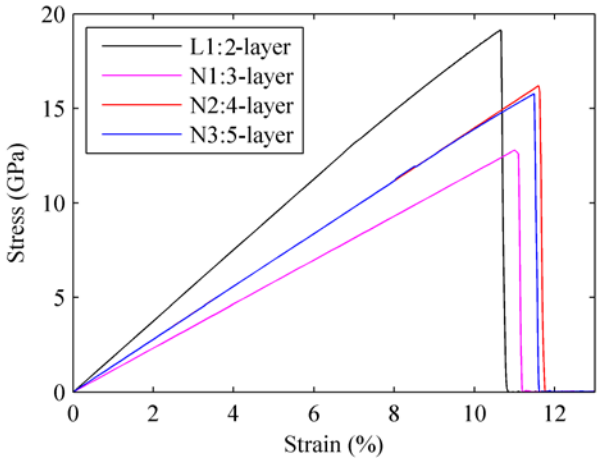

Figure 5. Stress-strain curves of GNHSs with different number of graphene layers.

The atomic configurations of different GNHSs have been tracked to identify the in-depth influence from the number of graphene layers. Similar as the above results, during the elastic deformation period, only stretched C-C bonds around the connecting regions are found (Figure 6a). When the stress passes the peak value, some of those stretched bonds are found to break, which leads to the failure of the structure (Figure 6b). The formation of monoatomic chains and rings and also inclined CNTs are found upon failure. In particular, the dangling graphene layers are found to adhere to each other forming a bi-layer or triple-layer graphene structure. As highlighted in Figure 6c, the distance between different dangling graphene layers is around 3.4 Å, which equals to the layer distance observed in multi-layer graphene. The emergence of the multi-layer graphene is originated from the shorter CNTs being utilized while establishing the model. After yielding, the dangling graphene layers will vibrate freely and the short distance between the two layers makes them easier to be adhered to each other through *van der Waals* force.

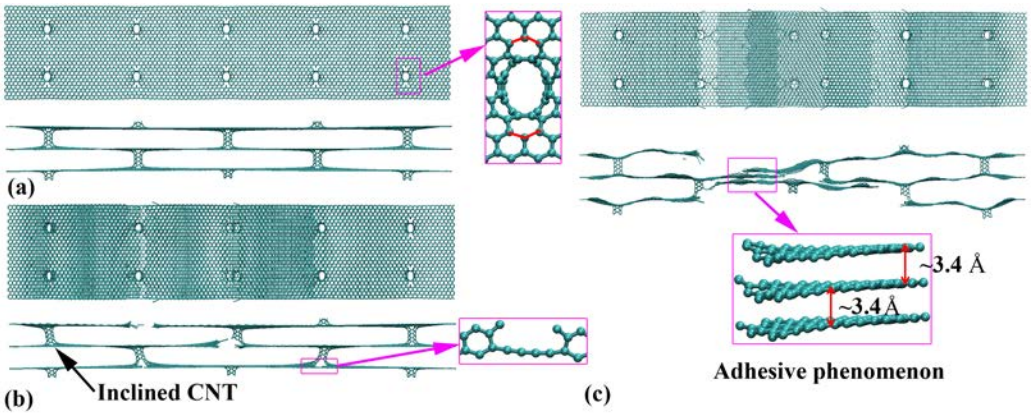

Figure 6. GNHS-N1 at the strain of: (a) 10.60%, inset shows the stretched carbon bonds; (b) 11.13%; (c) 11.30%, inset shows the adhered dangling graphene layers.

The incorporation of more graphene layers induces more complex deformation after yielding. In all three cases with three, four and five graphene layers, we found the fracture starts from the top layer and then propagates to the underneath layer. The existences of graphene layers have led to an easy formation of multi-layered graphene after failure (Figure 7b and 7d). For example, the residual atomic chain between graphene and CNT is found to be bended by the strong *van der Waals* interactions between the graphene layers (inset of Figure 7b).

To further investigate the structure influence on the mechanical properties of the hybrid structure, we also examine the tensile properties of GNHS with multi-walled CNTs (see inset of Figure 8a).

For the sample with a similar size as GNHS-L3 (length of 25.5 nm, width × height = 5.8 × 3.5 nm^2), a much higher Young's modulus (256.9 GPa) and yield strength (25.4 GPa) are estimated. As shown in Figure 8b, the failure of the structure is observed around the two outer CNTs in one end of the GNHS. After yielding, many monoatomic chains are formed at the fracture region. Particularly, it is found that only the outer CNTs have been split due to the tensile strain and the inner CNTs appears almost unchanged. Unlike the hybrid structures with SWNTs, no local bucking of the graphene layers is observed for the sample with multi-walled CNTs after yielding.

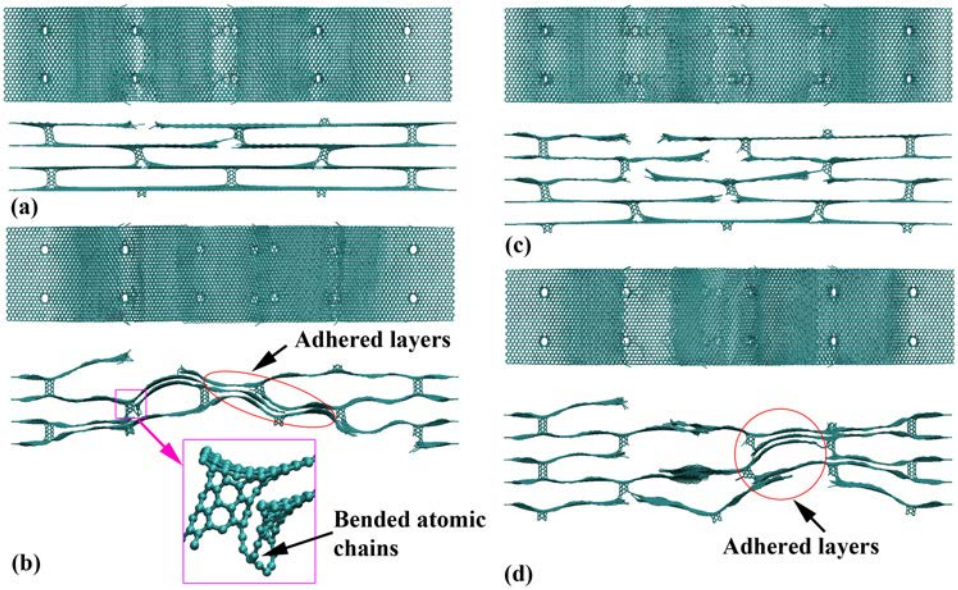

Figure 7. GNHS-N2 at the strain of: (a) 11.65%, (b) 12.63%, inset shows the bended atomic chains due to the *van der Waals* interactions between the adhered graphene layers; GNHS-N3 at the strain of: (c) 11.59%, (d) 11.87%.

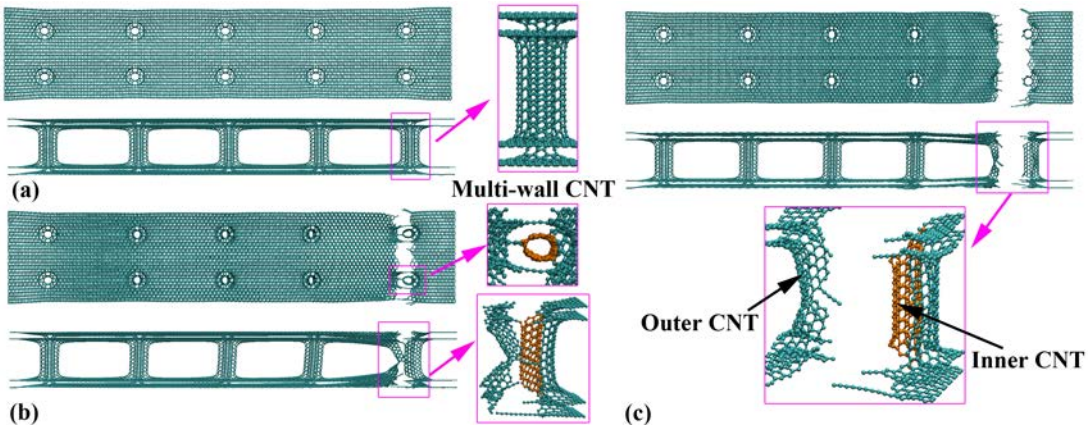

Figure 8. GNHS with multi-walled CNTs at the strain of: (a) 9.4%, inset shows a multi-walled CNT-graphene junction; (b) 10.1%, inset shows the deformation around the multi-walled CNT-graphene junctions; (c) 10.15%, inset shows the fracture of the outer CNTs.

Before concluding, we summarize the estimated tensile properties from all tested hybrid structures as listed in Table 1. Basically, Young's modulus and yield strength decrease with the increasing CNT length but have no strong relation with the number of graphene layers. In the other hand, the CNT length exerts marginal influence to the yield strain, and the increase of graphene layer number intends to increase the yield strain. In addition, comparing with its counterpart with SWNTs, the GNHS with multi-walled CNTs exhibits a much higher Young's modulus and yield strength, and a lower yield strain.

Table 1. Summary of Young's modulus, yield strength and yield strain for all considered graphene nanotube hybrid structures.

Different GNHSs		Young's modulus (GPa)	Yield strength (GPa)	Yield strain (%)
Bi-layer; SWNT's lengths L1-L6 (Å)	L1: 24.9	187.9	19.2	10.7
	L2: 30.3	159.9	16.3	10.6
	L3: 35.6	138.8	14.1	10.6
	L4: 40.9	121.7	12.4	10.6
	L5: 46.3	107.6	10.9	10.5
	L6: 51.9	96.2	9.7	10.5
Graphene layer number N1-N3	N1: 3	116.3	12.8	11.0
	N2: 4	139.6	16.2	11.6
	N3: 5	138.6	15.9	11.5
Multi-wall CNTs		256.9	25.4	9.9

Conclusions

Basing on large-scale MD simulations, we have examined the mechanical properties of graphene nanotube hybrid structures. It is found that the increase of CNT's length will induce a higher Young's modulus and yield strength, together with ignorable impacts to the yield strain of the hybrid structure. Whereas, no strong correlation is found between the number of graphene layers and Young's modulus and yield strength, though more graphene layers intends to lead to a higher yield strain. The presence of multi-wall CNTs are found to greatly strengthen the hybrid structure, which results in a much higher Young's modulus and yield strength. All studied hybrid structures exhibit a brittle behavior and the stretched carbon bonds are observed around the connecting regions between graphene and CNT during the elastic deformation period. Specifically, affluent formations of monoatomic chains and rings are found at the fracture region. For the hybrids structures with short CNT pillars, the dangling graphene layers will adhere to each other to form a multi-layered graphene after failure driven by *van der Waals* force. This study provides an in-depth understanding of relationship between the mechanical performance of the hybrid structures and their structures, which will shed lights on the design and also the applications of carbon-based nanostructures.

Acknowledgment

Supports from the ARC Discovery Project (DP130102120), the High Performance Computer resources provided by the Queensland University of Technology are gratefully acknowledged.

References

Brenner, D. W., O. A. Shenderova, J. A. Harrison, S. J. Stuart, B. Ni and S. B. Sinnott (2002). A second-generation reactive empirical bond order (REBO) potential energy expression for hydrocarbons *Journal of Physics: Condensed Matter* **14**, 783.

Chaste, J., A. Eichler, J. Moser, G. Ceballos, R. Rurali and A. Bachtold (2012). A nanomechanical mass sensor with yoctogram resolution *Nature Nanotechnology* **7**, 301-304.

Coluci, V. R., D. S. Galvao and A. Jorio (2006). Geometric and electronic structure of carbon nanotube networks:'super'-carbon nanotubes *Nanotechnology* **17**, 617.

De Volder, M. F., S. H. Tawfick, R. H. Baughman and A. J. Hart (2013). Carbon nanotubes: present and future commercial applications *Science* **339**, 535-539.

Dellinger, A., Z. Zhou, J. Connor, A. Madhankumar, S. Pamujula, C. M. Sayes and C. L. Kepley (2013). Application of fullerenes in nanomedicine: an update *Nanomedicine* **8**, 1191-1208.

Diao, J., K. Gall and M. L. Dunn (2004). Atomistic simulation of the structure and elastic properties of gold nanowires *Journal of the Mechanics and Physics of Solids* **52**, 1935-1962.

Dimitrakakis, G. K., E. Tylianakis and G. E. Froudakis (2008). Pillared graphene: a new 3-D network nanostructure for enhanced hydrogen storage *Nano Letters* **8**, 3166-3170.

Du, F., D. Yu, L. Dai, S. Ganguli, V. Varshney and A. Roy (2011). Preparation of tunable 3D pillared carbon nanotube–graphene networks for high-performance capacitance *Chemistry of Materials* **23**, 4810-4816.

Gere, J. and S. Timoshenko (1999). Mechanics of Materials, Cheltenham, UK: Stanley Thornes.

Hernández-Ferrer, J., P. Laporta, F. Gutiérrez, M. D. Rubianes, G. Rivas and M. T. Martínez (2014). Multi-walled carbon nanotubes/graphene nanoribbons hybrid materials with superior electrochemical performance *Electrochemistry Communications* **39**, 26-29.

Hoover, W. G. (1985). Canonical dynamics: Equilibrium phase-space distributions *Physical Review A* **31**, 1695-1697.

Kis, A., G. Csanyi, J.-P. Salvetat, T.-N. Lee, E. Couteau, A. Kulik, W. Benoit, J. Brugger and L. Forro (2004). Reinforcement of single-walled carbon nanotube bundles by intertube bridging *Nature Materials* **3**, 153-157.

Lee, J., V. Varshney, J. S. Brown, A. K. Roy and B. L. Farmer (2012). Single mode phonon scattering at carbon nanotube-graphene junction in pillared graphene structure *Applied Physics Letters* **100**, 183111-183111-183114.

Liu, B.-T. and H.-L. Kuo (2013). Graphene/silver nanowire sandwich structures for transparent conductive films *Carbon* **63**, 390-396.

Loh, G. C., E. H. T. Teo and B. K. Tay (2011). Interpillar phononics in pillared-graphene hybrid nanostructures *Journal of Applied Physics* **110**, 083502.

Matsumoto, T. and S. Saito (2002). Geometric and electronic structure of new carbon-network materials: Nanotube array on graphite sheet *Journal of the Physical Society of Japan* **71**, 2765.

Nosé, S. (1984). A unified formulation of the constant temperature molecular dynamics methods *The Journal of Chemical Physics* **81**, 511.

Novaes, F. D., R. Rurali and P. Ordejón (2010). Electronic transport between graphene layers covalently connected by carbon nanotubes *ACS Nano* **4**, 7596-7602.

Novoselov, K., V. Fal, L. Colombo, P. Gellert, M. Schwab and K. Kim (2012). A roadmap for graphene *Nature* **490**, 192-200.

Odedairo, T., J. Ma, Y. Gu, J. Chen, X. S. Zhao and Z. Zhu (2014). One-pot synthesis of carbon nanotube-graphene hybrids via syngas production *Journal of Materials Chemistry A* **2**, 1418-1428.

Paul, R. K., M. Ghazinejad, M. Penchev, J. Lin, M. Ozkan and C. S. Ozkan (2010). Synthesis of a Pillared Graphene Nanostructure: A Counterpart of Three-Dimensional Carbon Architectures *Small* **6**, 2309-2313.

Plimpton, S. (1995). Fast parallel algorithms for short-range molecular dynamics *Journal of Computational Physics* **117**, 1-19.

Sihn, S., V. Varshney, A. K. Roy and B. L. Farmer (2012). Prediction of 3D elastic moduli and Poisson's ratios of pillared graphene nanostructures *Carbon* **50**, 603-611.

Varshney, V., S. S. Patnaik, A. K. Roy, G. Froudakis and B. L. Farmer (2010). Modeling of thermal transport in pillared-graphene architectures *ACS Nano* **4**, 1153-1161.

Verlet, L. (1967). Computer 'experiments' on classical fluids. I. Thermodynamical Properties of Lennard-Jones Molecules *Physical Review* **159**, 98-103.

Wang, J. (2005). Carbon-nanotube based electrochemical biosensors: A review *Electroanalysis* **17**, 7-14.

Xia, K., H. Zhan, Y. Wei and Y. Gu (2014). Tensile properties of a boron/nitrogen-doped carbon nanotube–graphene hybrid structure *Beilstein Journal of Nanotechnology* **5**, 329-336.

Xu, L., N. Wei, Y. Zheng, Z. Fan, H.-Q. Wang and J.-C. Zheng (2012). Graphene-nanotube 3D networks: intriguing thermal and mechanical properties *Journal of Materials Chemistry* **22**, 1435-1444.

Zhan, H. F. and Y. T. Gu (2011). Atomistic exploration of deformation properties of copper nanowires with pre-existing defects *CMES: Computer Modeling in Engineering & Sciences* **80**, 23-56.

Zhan, H. F., K. Xia and Y. T. Gu (2013). Tensile properties of graphene-nanotube hybrid structures: a molecular dynamics study *International Journal of Computational Materials Science and Engineering* **02**, 1350020.

Zhang, Y., C. Wang, Y. Cheng and Y. Xiang (2011). Mechanical properties of bilayer graphene sheets coupled by sp^3 bonding *Carbon* **49**, 4511-4517.

Zhao, M.-Q., X.-F. Liu, Q. Zhang, G.-L. Tian, J.-Q. Huang, W. Zhu and F. Wei (2012). Graphene/Single-Walled Carbon Nanotube Hybrids: One-Step Catalytic Growth and Applications for High-Rate Li–S Batteries *ACS Nano* **6**, 10759-10769.

Zhu, Y., L. Li, C. Zhang, G. Casillas, Z. Sun, Z. Yan, G. Ruan, Z. Peng, A.-R. O. Raji and C. Kittrell (2012). A seamless three-dimensional carbon nanotube graphene hybrid material *Nature Communications* **3**, 1225.

Zhu, Y., S. Murali, W. Cai, X. Li, J. W. Suk, J. R. Potts and R. S. Ruoff (2010). Graphene and graphene oxide: synthesis, properties, and applications *Advanced Materials* **22**, 3906-3924.